Nano Energy 51 (2018) 162–172

Contents lists available at ScienceDirect

Nano Energy

journal homepage: www.elsevier.com/locate/nanoen

Full paper

Novel augmented reality interface using a self-powered triboelectric based virtual reality 3D-control sensor

Tao Chen[a,b,c,d], Mingyue Zhao[b,c,d,e], Qiongfeng Shi[b,c,d,e], Zhan Yang[a], Huicong Liu[a,*], Lining Sun[a], Jianyong Ouyang[f], Chengkuo Lee[b,c,d,e,g,**]

[a] *Jiangsu Provincial Key Laboratory of Advanced Robotics & Collaborative Innovation Center of Suzhou Nano Science and Technology, Soochow University, Suzhou 215123, PR China*

[b] *Department of Electrical and Computer Engineering, National University of Singapore, 4 Engineering Drive 3, 117576, Singapore*

[c] *Center for Intelligent Sensors and MEMS, National University of Singapore, E6 #05-11F, 5 Engineering Drive 1, 117608, Singapore*

[d] *Hybrid-Integrated Flexible (Stretchable) Electronic Systems Program, National University of Singapore, E6 #05-4, 5 Engineering Drive 1, 117608, Singapore*

[e] *NUS Suzhou Research Institute (NUSRI), Suzhou Industrial Park, Suzhou 215123, PR China*

[f] *Department of Materials Science and Engineering, National University of Singapore, 9 Engineering Drive 1, 117574, Singapore*

[g] *NUS Graduate School for Integrative Science and Engineering, National University of Singapore, 117456, Singapore*

ARTICLE INFO

Keywords:
Triboelectric effect
Self-powered
3D control sensor
Augmented reality
Virtual reality

ABSTRACT

Triboelectric nanogenerators and sensors have been widely adopted for diversified energy harvesting and sensing applications, but the demonstrations of 3D information sensing and controlling are very limited. In this paper, we present a novel self-powered virtual reality 3D-control sensor (VR-3D-CS) based on triboelectric mechanism for controlling the attitude (both the position and rotation) of object in 3D virtual space. This innovative, cost-effective, simple-designed sensor has a symmetric 3D structure with eight separated sensing electrodes and two touching spheres as the interactive interface with human fingers for 3D force information sensing and VR controlling. Based on the coupling effect of triboelectrification and electrostatic induction, the VR-3D-CS generates different electric output signals in response to different operation manner that can be used to control the attitude of objects in 3D virtual space. The symmetrical 3D configuration design of the sensor enables the detection of 3D force from both the normal direction and shear direction. By employing vector properties of force and signal analysis from the eight sensing electrodes, detection of six-axis directions in 3D space is achieved by triboelectric mechanism for the first time. The VR-3D-CS has been demonstrated to be able to detect normal force in the range of 0–18 N. It can resolve the shear force direction with step resolution of at least 15°. Besides, due to the positive output voltage and low internal impedance, the VR-3D-CS is readily compatible with commercial portable signal processing system for signal analysis and controlling. Demonstration of the VR-3D-CS as interactive interface for Augmented Reality (AR) control is successfully realized. The robust structure, stable output performance and self-powered sensing property enable the device as an ideal human machine interface towards AR interface, batteryless and energy saving applications.

1. Introduction

Developing a multisource information fusion and interactive system is important for applications in virtual reality (VR) and augmented reality (AR) [1–4]. Especially, the real time understanding of human interaction intentions from related information has become major technology trend of the VR and AR system. As a subset of AR, VR provides completely virtual information that is mainly for creating a sense of immersion. AR is based on the reality that superimposes virtual scenes with reality and provides more real information. In VR and AR information collection system, various types of sensors as the interactive tools are the key components. At present, the mainstream technologies of human machine interactions can be categorized into eye movement tracking, mark point tracking, optical sensor interacting and tactile sensor interacting system [5–7]. Eye movement tracking simulates the visual effect in reality to complete some menu operations by acquiring changes in eyeballs, surrounding features, or projecting infrared to iris to extract features. For mark point tracking, the information of mark point is saved in advance and then the image recognition technology is used to find and identify the mark to combine

* Corresponding author.
** Corresponding author at: Department of Electrical and Computer Engineering, National University of Singapore, 4 Engineering Drive 3, 117576, Singapore.
E-mail addresses: hcliu078@suda.edu.cn (H. Liu), elelc@nus.edu.sg (C. Lee).

https://doi.org/10.1016/j.nanoen.2018.06.022
Received 3 April 2018; Received in revised form 22 May 2018; Accepted 7 June 2018
Available online 18 June 2018
2211-2855/ © 2018 Elsevier Ltd. All rights reserved.

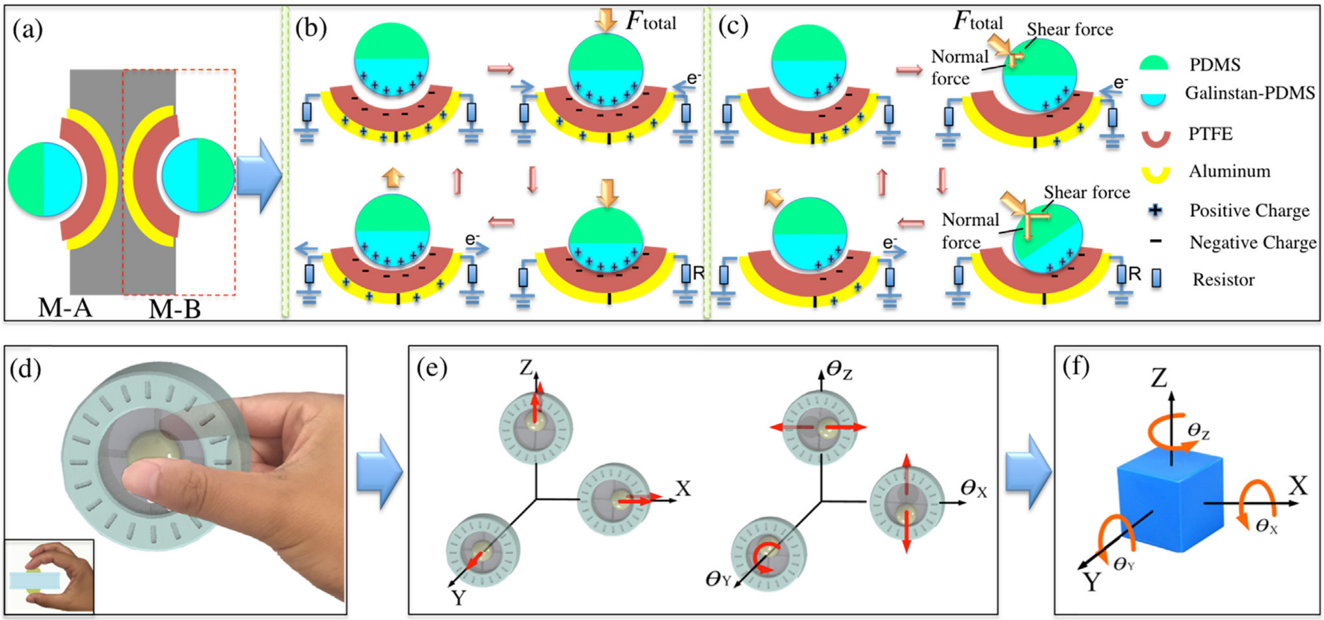

Fig. 1. (a) The symmetrical structure of the self-powered sensor. (b) Working mechanism of the 3D self-powered sensor under normal force based on the electric field change with the applied force. (c) Working mechanism of the 3D self-powered sensor under tilted force. (d) Operation chart of the 3D attitude-control sensor. (e) The relationship between the detection principle of 3D attitude-control sensor and (f) the motion of the object in 3D virtual space.

the animation and display. Optical sensors or tactile sensors are controlled by translating the optical signals (images) and mechanical signals into electrical signals. Compared with the first three types of technologies, the tactile sensors have the advantages of high sensitivity, good dynamic performance, small size, easy to wear and so on [8,9], especially in the intent perception of human intuitive commands in the AR applications.

Along the development of AR, portable, low power and low cost tactile sensors have become the development trend of interactive tools. However, in some AR applications such as virtual assembly, games, and AR home designer, traditional tactile sensors are complex and inconvenient. Over the years, major research efforts have been focused on motion sensing mechanisms including optical and mechanical for the optimization of interacting system [10–14]. Mechanical sensing mechanism can directly convert a mechanical trigger into electric signal for detection of motion, vibration and physical touching. But it is still difficult to implement a lightweight, simple, good interactive system. In addition, a common limitation is that most of these sensors require an external power source, which poses challenges to longevity and mobility of the sensor. In recent years, a number of self-powered sensors based on triboelectric nanogenerators (TENGs) were extensively investigated and developed [15–21]. By harvesting the mechanical energy from its working environment, the TENG based sensors are able to work independently without an external power source. On the basis of coupling effect between triboelectrification and electrostatic induction, they have been adopted for various physical/chemical sensing applications such as detecting mercury ions, changes of magnetic field, flow field and spatial displacement [22–28].

In particular, TENG for tactile sensing has received increasing research interests in the last few years [29–34]. TENGs can achieve high output power density, enabling diversified applications of tactile sensors in wireless systems, portable electronics, biomedical microsystems and self-powered nanosensors [35–43]. By transforming mechanical energy into electrical energy, self-powered TENG based touch sensors can generate voltage, current or charge to indicate the property of applied force, i.e. normal force component and shear force component. The working modes of TENG based sensors are rather diverse and could also be applied to harvest most of conventional mechanical/kinetic motions in our daily life [44–51]. For example, Zhu et al. reported a triboelectric tactile sensor that can achieve high sensitivity of 44 mV Pa^{-1} in low pressure range ($<$ 0.15 kPa) [52]. Yi et al. presented a self-powered, single-electrode-based triboelectric sensor (TES) to accurately detect the movement of a moving object/body in two dimensions [53]. Shi et al. proposed a flexible liquid-solid interface triboelectric based microfluidic sensor for pressure/force sensing and finger bending monitoring [54]. Meng et al. demonstrated a self-powered touch sensor with micro-patterned PDMS to achieve high output performance [55]. Along the years of research, normal force components were characterized by TENG based touch/tactile sensors with high sensitivity and robust performance [56–58]. However, general applied forces on the sensors are composed of normal and shear components. The shear force components with direction information are barely studied by TENG based sensors in the 2D applications. Furthermore, limitation of structure design of the previous TENG based sensors inhibits their applications for 3D parameter detection. To date, no relevant research has been conducted using the TENG as a self-powered 3D-control sensor in AR interactive system.

In this paper, we present a self-powered, triboelectric based virtual reality 3D-control sensor (VR-3D-CS) by the coupling of contact electrification and electrostatic induction. The VR-3D-CS has a novel structure design of two opposite touch spheres and separated sensing electrodes for 3D force information sensing and controlling. By moving two spheres toward same directions or opposite directions, 3D space coordinates (X, Y, Z and θ_X, θ_Y, θ_Z) can be detected and controlled. Six-axis directions in 3D space are detected by triboelectric mechanism for the first time. When the sphere under external force approaches or leaves the triboelectric layer, it will change the distribution of the local electric field, which would lead to a flow of electrons moving back and forth between the electrodes and ground. This work analyzed the working mechanism of VR-3D-CS according to the electric field theory and characterization of the device for normal force and shear force detection. Using the vector properties of forces, the attitude-control function in 3D space is realized. The sensor generates electric output signals in response to different operation manner for attitude-control of objects in 3D virtual space. To demonstrate the practical application, experiment of virtual assembly controlled by this VR-3D-CS for AR interface is conducted and successfully realized. The VR-3D-CS presented in this work shows robust structure and stable output performance, enabling itself as an ideal human machine interface towards AR interface, batteryless and energy saving applications.

2. Experiment

2.1. Working mechanism

The symmetric VR-3D-CS is composed of two identical non-planar TENG sensing modules, named M-A and M-B as shown in Fig. 1(a). The single module consists of top semi-sphere touch point, bottom functional semi-sphere, polytetrafluoroethylene (PTFE) thin film, aluminum (Al) electrode and supporting structure. The bottom semi-sphere is made by mixing galinstan (eutectic alloy of 68.5% gallium, 21.5% indium and 10% tin by weight) with polydimethylsiloxane (PDMS). The galinstan-PDMS mixture functions as one triboelectric layer and conductive material [59]. The working mechanism of each module under normal force and titled force are shown in Fig. 1(b) and (c). Under the tilted force, the sensor can detect both the normal and shear force components simultaneously as shown in Fig. 1(c). The attitude-control principle of the sensor in 3D space is shown in Fig. 1(d-f). By the vector decomposition of the forces acted on spheres, the normal and shear forces on the two modules are depicted by Fig. 1(e). Through the combinational detection signals of the normal and shear forces, the 3D attitude-control of the object in the space (Fig. 1(f)) can be realized along six axes (X, Y, Z and θ_X, θ_Y, θ_Z) in the rectangular coordinate system (Fig. 1(e)). Therefore, how to detect normal and shear force is the primary part of this work. (See Supporting Information Movie 1)

Supplementary material related to this article can be found online at http://dx.doi.org/10.1016/j.nanoen.2018.06.022.

The basic qualitative working mechanism of the self-powered sensor under normal force is shown in Fig. 1(b). Because of the work function difference between galinstan and PTFE [60,61], a physical contact between the two dielectric films with distinct electron affinity creates oppositely charged surfaces. Negative charges will transfer from galinstan surface to PTFE, which causes the PTFE surface carries net negative charge. Due to Coulomb's law, the total charge induced in the Al electrode is contributed by the negative charge on PTFE surface. When the force is applied, the positive charge on galinstan is attracted significantly by the negative charge on PTFE in the contacting area. The electric field generated by the positive charge is also enhanced under the contacting area. Corresponding charge pair would be induced in the Al electrode. After force is released and the deformed structure recovers to initial shape, the electric field is weakened and the charge pairs are also reduced. When the electrode is connected to ground with a resistor in Fig. 1(b), the induced positive charge in the electrode would flow to the ground to keep electrostatic equilibrium.

Optimizing the contact area and structure of the TENG can effectively increase the overall triboelectric charge density. Thus, the structure of PTFE is designed to be a hemispherical bottom, as shown in Fig. 1(a-b). The contact area A of galinstan-PDMS sphere and PTFE film is an approximate circle on the model.

Based on the contact area between two different materials given by Hertz hypothesis, the area can be calculated as:

$$S_A = \pi \left[\frac{3}{4} \frac{R_1 R_2}{R_2 - R_1} \left(\frac{1-\upsilon_1^2}{E_1} + \frac{1-\upsilon_2^2}{E_2} \right) F \right]^{\frac{2}{3}} \tag{1}$$

where S_A is the contact area of galinstan-PDMS sphere and PTFE film under the force, E_1 and E_2 are the modulus of elasticity for galinstan-PDMS mixture and PTFE film, υ_1 and υ_2 are the Poisson's ratios, respectively. F is the applied force on the top dome and R_1 and R_2 is the radius of the PDMS sphere and PTFE layer, respectively. Because the galinstan is still liquid phase in the galinstan-PDMS mixture, the modulus of elasticity is referred to the value of PDMS.

The surface charge density, σ of galinstan-PDMS and PTFE contacting area is given by [61]:

Table 1
Material parameters.

Parameter name	Symbol	Value
Sphere diameter	R	5×10^{-3} m
PTFE sheet thickness	d	1×10^{-4} m
galinstan-PDMS mixture elastic modulus	E_1	0.75 MPa
PTFE sheet elastic modulus	E_2	1.5 GPa
galinstan-PDMS mixture Poisson's ratio	υ_1	0.5
PTFE sheet Poisson's ratio	υ_2	0.41
Charge of electron	e	-1.602×10^{-19} C
Vacuum permittivity	ε_0	8.854×10^{-12} F m^{-1}
Relative permittivity of PTFE	ε_r	2.1
Number of surface states	D_s	7×10^{10} eV^{-1} cm^{-2}
Work function of PTFE	W_p	5.75 eV
Work function of Gallium	W_m	4.25 eV
Work function of Aluminum	W_{Al}	4.08 eV
Work function of Gold	W_{Au}	5.1 eV

$$\sigma = eD_s(W_m - W_p) \tag{2}$$

where e is the charge of an electron, D_s is the number of surface states per unit area and unit energy. W_m and W_p are the work functions of the metal gallium and PTFE. Gallium's work function has been used to represent the work function of galinstan, for gallium is the main part of the eutectic alloy. The charge amount Q generated on galinstan surface of the contacting area is then derived as:

$$Q = \sigma \bullet A \tag{3}$$

Combing Eqs. (1)–(3), the generated charge can be calculated. The material parameters in the equation can be obtained in Table 1 from the literature [61–67].

It is assumed that the sphere can achieve a spherical contact area of chord length of 10 mm under normal force. The theoretical maximum normal force is calculated as 18 N through Eq. (1). The relationship of contacting area and induced charge Q against with applied force is almost linear in the range of 0–18 N. Therefore, the normal force can be measured through above-mentioned mechanism.

The value and direction of shear force component can be simultaneously measured by the design of four quadrant electrodes as shown in Fig. 1(c) and Fig. 2. As the applied force changes, the four electrodes under the PTFE sheet perceive the change distribution. The PDMS film, circling around the sphere, confines the sphere position in the center. The force applied on the top dome of the sensor can be resolved into two parts, as shown in Fig. 2(a). The force contributes to form the contacting area between the galinstan-PDMS sphere and PTFE, which induces outputs of corresponding electrodes. When the force is released, the PDMS film will push the sphere back to initial position. To demonstrate the working mechanism, a shear force is applied at an angle θ to the x axis. The electric field on E1 and E4 generated by galinstan in the contacting area is enhanced comparing with the initial electric field. Therefore, the current flows from E1 and E4 to the ground. When the force is released, the electric fields are back to the initial state and

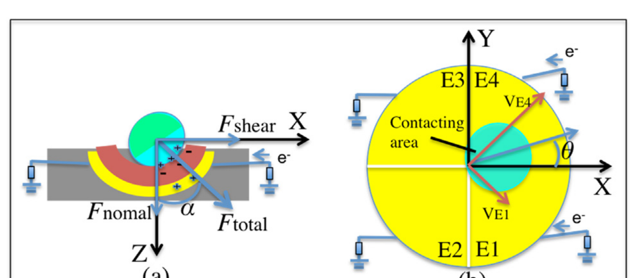

Fig. 2. (a) Force component analysis acting on self-powered sensor. (b) The structure form with four electrodes and working mechanism for shear force detecting.

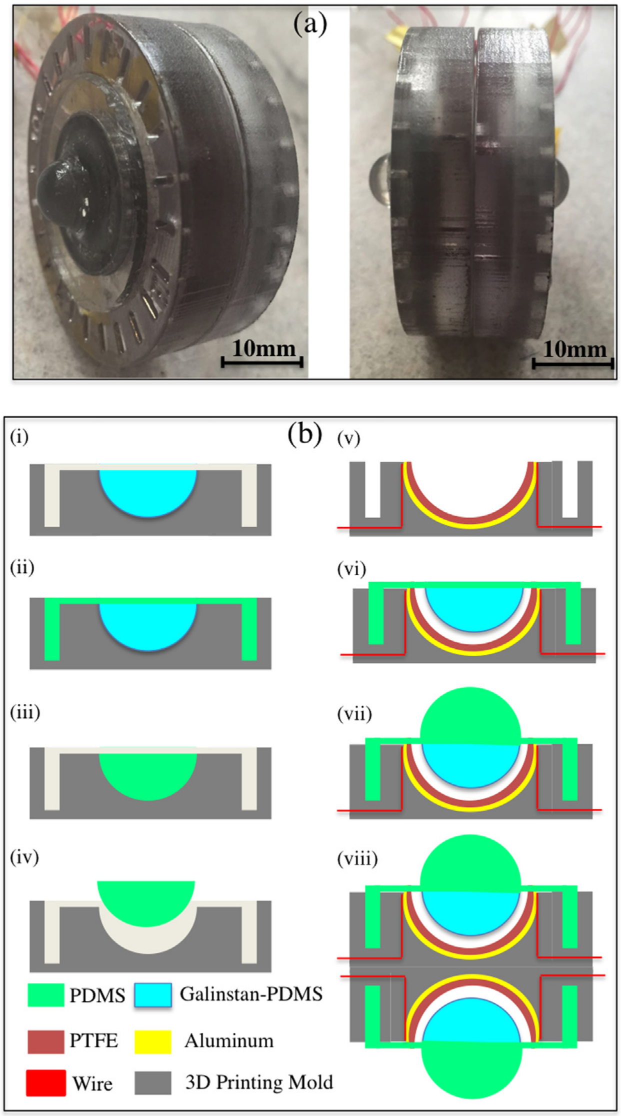

Fig. 3. Fabrication process of the 3D self-powered sensor.

current flows in the opposite direction. Since charge output, open circuit voltage and short circuit current of each electrode have proportional relationship with force components shared on the corresponding electrodes, force magnitude and direction can be determined by outputs of different electrodes. Fig. 2(b) is a projection of a spherical surface of PTFE at the bottom. The X and Y axes coincide with the two lines of the E4 sector, respectively.

For the sensor application, the amplitude of the output voltage of shear force is represented by

$$V_{shear} = \sqrt{V_{E1}^2 + V_{E4}^2} \tag{4}$$

As shown in Fig. 2(b), the horizontal angle θ, between the x-axis positive direction and the shear force, is derived by

$$\theta = 45° - tan^{-1}\frac{V_{E1}}{V_{E4}} \tag{5}$$

2.2. Fabrication process of the self-powered sensor

The photos of sensor are shown in Fig. 3(a). The detail fabrication process is shown in Fig. 3(b). (i) The PDMS (Sylgard 184 Dow Corning, USA) is mixed with cross-linker by the weight ratio of 10:1. The solution is then mixed with galinstan (Changsha Santech Materials, China) by the weight ratio of 1: 6.44 in the crucible, and then the mixture is fully stirred and grinded until the galinstan is completely mixed with the liquid PDMS. Then the mixture is poured into a 3D printing mold. (ii) Then keep on pouring pure PDMS into the mold to form the supporting structure. The mold is cured in the oven immediately for 60 min under 70 °C to solidify the PDMS to form the bottom semi-sphere and supporting structure. The cured structure of galinstan and PDMS is shown in Fig. S1 (Supporting Information). (iii) Next step, keep on pouring pure PDMS into another same mold to form the top sphere. (iv) After the structure is degassed and cured in the oven for 60 min under 70 °C, the top sphere is taken out of the mold to spare. (v) The frame of the sensor is fabricated with 3D printing technology. The PTFE sheet and Al electrode are placed on bottom. (vi) The structure fabricated by step (ii) is then demolded and packaged into frame. (vii) The PDMS top sphere is bonded on the bottom sphere by PDMS-PDMS bonding method. (viii) Two modules are attached back to back together to form a complete sensor.

3. Results and discussion

3.1. Characterization of normal force detection

From the above analysis, the force acted on the sensor contains normal force and shear force component. The shear force has a proportional relationship with normal force. Therefore, the detection of normal force is necessary. Because of the symmetrical structure design, the VR-3D-CS will be detected for each module. First, the hammer of the force gauge is set to be exact contact with the vertex of sphere without yielding any deformation. Because the sphere radius is 5 mm, the force gauge is set to run up and down 50 cycles with a displacement of 6 mm to make sure the bottom PTFE layer is sufficiently charged. The testing setup is shown in Fig. 4(a). Fig. 4(b-d) shows the E1 and E1′ outputs performance of module A and B, respectively.

It is easy to find out that the module has the output performance in open-circuit voltage (maximum 65 V), charge output (maximum 19.3 nC) and short circuit current (peak-peak maximum 0.2 μA). Open circuit voltage, charge output measurements of the devices are conducted with Electrometer (Keithley 6514). Short circuit current is measured by Stanford SR570. The normal force applying on the devices is generated by force gauge (Mecmesin 2.5-I, Germany).

Fig. 4(e–g) shows the relationship of output performance against the applied force. These outputs show good linear range from 0 to 18 N, which is consistent with the theoretical and simulation results. The open circuit voltage, output charge and short circuit current sensitivity are 3.6 V N^{-1}, 1.1 nC N^{-1} and 11.1 nA N^{-1}, respectively. This linear property is quite useful in the self-powered sensor application for normal force measurement. The open circuit voltage outputs of four electrodes in 0–18 N linear range are shown in Fig. 4(h)–(i). The four curves show similar linear property and comparable output amplitude comparing with single electrode. The cycling stability of VR-3D-CS under normal force of 10 N is tested as shown in Fig. 4(j)–(m). The consistent voltage can be maintained after 10,000 loading–unloading cycles, implying long working life and reliability of VR-3D-CS.

3.2. Characterization of shear force detection

To make the testing results reliable, the force is applied at the limitation of finger capability on the top dome of the sensor. Thumb and index fingers keep the same amplitude around 10 N and same vertical angle in different horizontal directions. First, the shear forces along the direction of X and Y axes (0°, 90°, 180°, 270°) are detected, as shown in Fig. 5. Due to the low input impedance (1 MΩ) of the oscilloscope (Agilent DSO-X 3034 A) comparing to 200 TΩ of Keithley 6514 electrometer, the output voltages are only a small portion of the open-circuit. It can be used to resolve the horizontal direction of the shear force since output voltages are still proportional to the force amplitude.

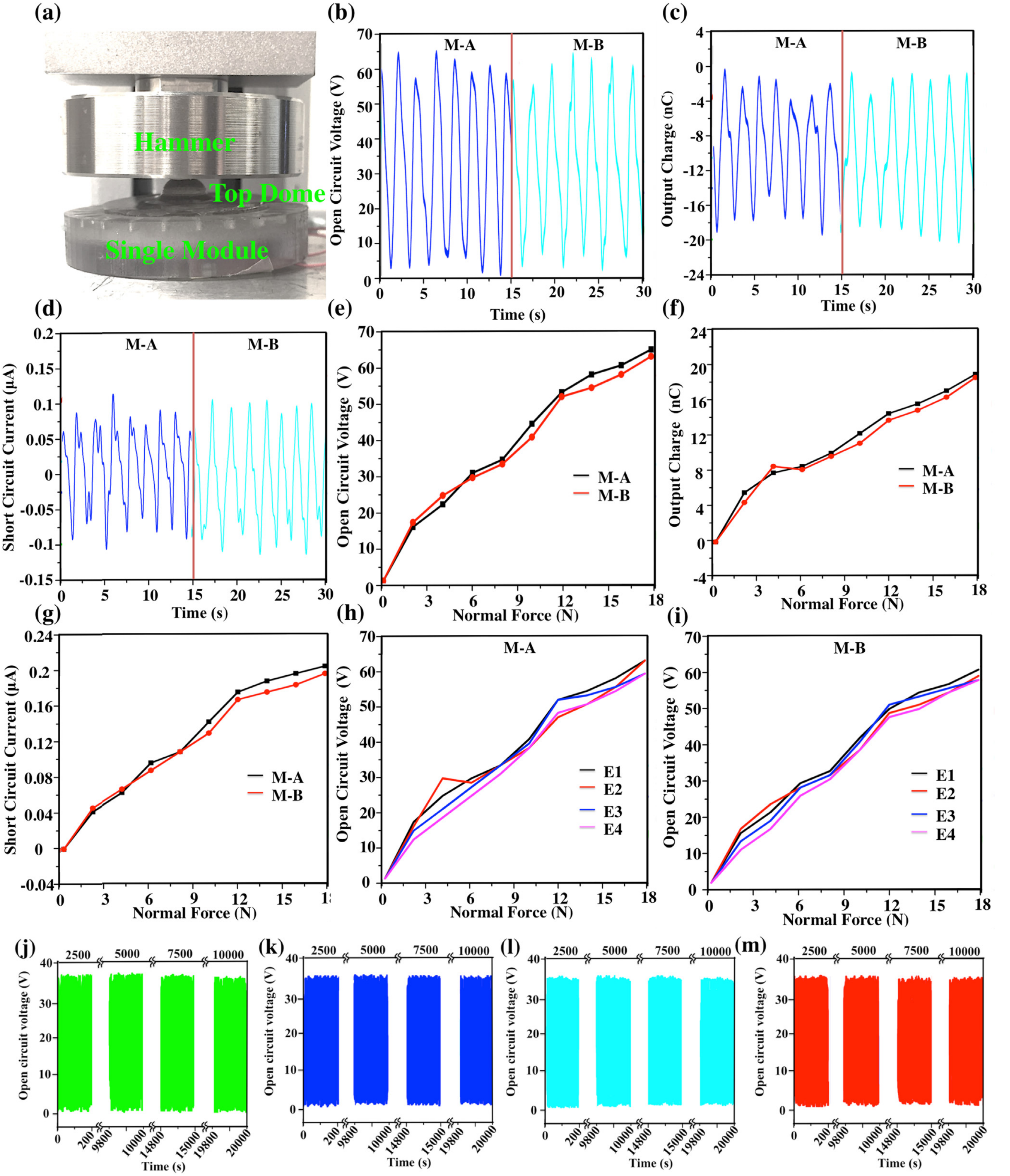

Fig. 4. (a) Testing setup of normal force detection. (b) The open circuit voltage under 18 N normal force. (c) The output charge. (d) The short circuit current. (e) The open circuit voltage versus applied normal force. (f) The output charge versus applied normal force. (g) The short circuit current versus applied normal force. (h) The open-circuit voltage outputs of four-electrode configuration (M-A). (i) The open-circuit voltage outputs of four-electrode configuration (M-B). (j) The reliability test of E1 under pressure of 10 N. The voltage change curves were recorded after each 2500 cycles and 100 cycles of data were presented in each recording. (k)-(m) The reliability test of E2-E4.

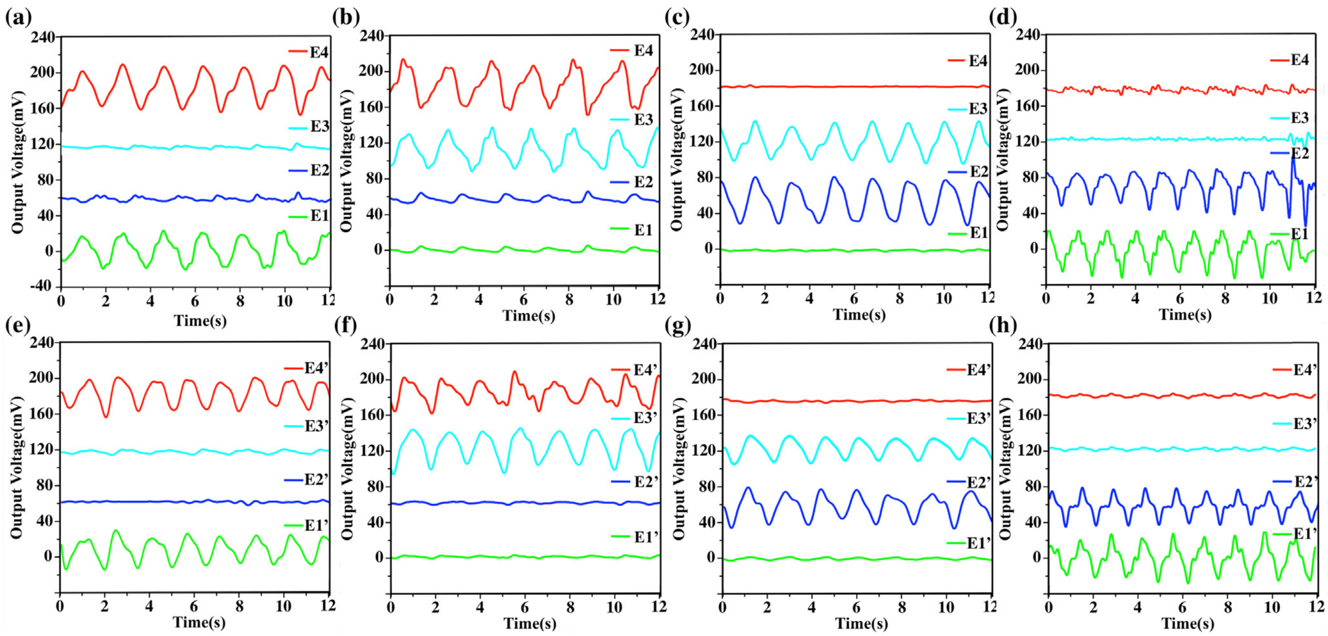

Fig. 5. (a-d) Output voltage waveform of M-A by repetitive motions in 0°, 90°, 180°, 270° directions. (e-h) Output voltage waveform of M-B by repetitive motions in 0°, 90°, 180°, 270° directions.

The repetitive motion of finger is repeated for more than 5 cycles and the peak-peak output voltages are calculated to elevate the accuracy and reliability of measurements.

To differentiate the output voltage waveforms of each electrode, E2(E2′), E3(E3′) and E4(E4′) have the positive voltage offsets of 60 mV, 120 mV and 180 mV, respectively. Fig. 5 shows the zoom-in figure of each motion of 0°, 90°, 180°, 270° directions. In Fig. 5(a) and (e), the amplitudes of E2(E2′) and E3(E3′) are nearly zero, while the value of E1(E1′) and E4(E4′) are larger values because the contacting area are all on E1(E1′) and E4(E4′). E1(E1′) and E4(E4′) are almost the same due to the same contacting area on each electrode during the operation period. There are small differences in the magnitudes due to the fabrication deviations. In the same way, the 90° direction is characterized by the same value of E3(E3′) and E4(E4′) and the minimum value of E1(E1′) and E2(E2′). The 180° and 270° directions are analogous in turn as shown in Fig. 5(c), (g) and Fig. 5(d), (h).

From Eq. (5), it can be seen that the angle θ is calculated by the voltage amplitudes of two adjacent electrodes. In order to detect the resolution of the angle θ, the repetitive motion of finger is moving in different directions, respectively, increasing in units of 5°. Taking M-A

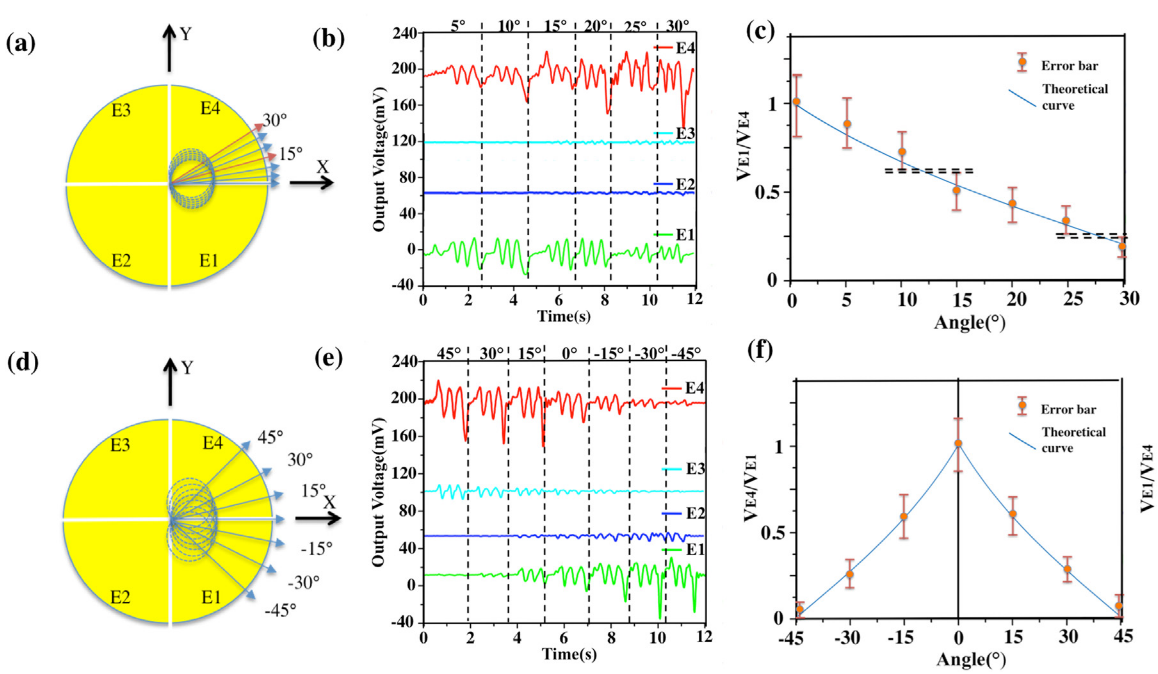

Fig. 6. (a) Repetitive motion of finger in different directions from 5° to 30°, increasing in units of 5°. (b) The voltage value of four electrodes corresponding to the operation of (a). (c) Relationship between the measurement curve with error bars of V_{E1}/V_{E4} and the theoretical curve. (d) Repetitive motion of finger in different directions from −45° to 45°, increasing in units of 15°. (e) The voltage value of four electrodes corresponding to the operation of (d). (f) Relationship between the measurement curve with error bars of V_{E1}/V_{E4} (0–45 °), V_{E4}/V_{E1} (-45°-0), and the theoretical curve.

as an example as shown in Fig. 6(a) and (b), the voltage value of E1 gradually decreases as the angle changes, and the voltage value of E4 increases because of the contacting area are increased. In order to calculated and plotted the average voltage ratio of V_{E1}/V_{E4} with error bar, we test the output voltage of each electrode and calculate the ratio for 15 times at every 5°. As shown in Fig. 6(c), it can be seen that at every 15°, the ratio value can be clearly distinguished without overlap area. Therefore, we defined that the shear force resolution detection has achieved a resolution of 15°.

To further verify the accuracy of the resolution, Fig. 6(d), (e), (f) shows the other 7 repetitive motions with the directions of − 45°, − 30°, − 15°, 0°, 15°, 30° and 45°, respectively. Fig. 6(f) shows the ratio value with error bar as the angle changes from − 45° to 45°, increasing in units of 15°. The error bars of 7 motions have no overlap area in the projection of ordinate. The sensor can accurately identify the direction of the shear force. In Fig. 2(b), the angle θ is defined as the acute angle between the x-axis positive direction and the shear force. So the ratio in Eq. (5) is changed to V_{E4}/V_{E1} when we need to analysis negative degrees (0 to − 45°). Therefore, the result shown in Fig. 6(f) is bilateral symmetry from 0° and the ordinates are V_{E1}/V_{E4} and V_{E4}/V_{E1}, respectively. When the angle exceeds − 45° or 45°, the calculation will change to the next pair of electrodes correspondingly.

In summary, the shear force direction can be detected by the self-powered sensor through differentiating the amplitudes and phases of the four outputs. This paper mainly embodies the control characteristic of the sensor. However, in order to increase the angle resolution and extend the sensor applications, the Al electrodes structure is optimized to change the voltage ratio V_{E1}/V_{E4} for increasing the resolution. Experimental results show that the resolution is improved (Supporting Information).

Fig. 7 shows the output results for the rotation motions of finger around the central axis of the single module. In Fig. 7(a), E1, E2, E3 and E4 have a time delay in turn. This delay shows the motion is a clockwise rotation. The rotation period is about 1 s. In Fig. 7(b), E1′, E2′, E3′ and E4′ also have a time delay in turn with a low frequency. In Figs. 7(c) and 7(d), E1(E1′), E2(E2′), E3(E3′) and E4(E4′) have a time advance in turn. This time advance shows the rotation is a counter-clockwise rotation. Therefore, besides shear force direction detecting, the VR-3D-CS is also able to detect the rotation direction and period of the finger motion. This greatly broadens the VR-3D-CS for more advanced control applications. In the next section, the role of rotation direction will be introduced.

3.3. Strategy and characterization of 3D attitude-control

At first, the kinematic analysis of the object in the rectangular coordinate system is studied. In 3D space, the transformation between different coordinate systems is the transformation of the different original points and coordinate axes. The rotation of the two coordinate systems can be regarded as a coordinate system that rotates three times to another coordinate system, and the three rotation angles are Euler angles in Eq. (6). Because the translation and scale transformation are simple, the rotation transformation in the rectangular coordinate system is considered for the convenience of attitude-control. And later experiment is carried out in the rectangular coordinate system. The attitudes of object in 3D space can be characterized by the 3D parameters (X, Y, Z and θ_X, θ_Y, θ_Z) in the rectangular coordinate system.

$$\begin{aligned} Euler(\theta_x,\theta_y,\theta_z) &= Rot(x,\theta_x)Rot(y,\theta_y)Rot(z,\theta_z) \\ &= \begin{bmatrix} 1 & 0 & 0 \\ 0 & cos\theta_x & sin\theta_x \\ 0 & -sin\theta_x & cos\theta_x \end{bmatrix} \begin{bmatrix} cos\theta_y & 0 & 0-sin\theta_y \\ 0 & 1 & 0 \\ sin\theta_y & 0 & cos\theta_y \end{bmatrix} \begin{bmatrix} cos\theta_z & sin\theta_z & 0 \\ -sin\theta_z & cos\theta_z & 0 \\ 0 & 0 & 1 \end{bmatrix} \end{aligned} \tag{6}$$

In view of the above sections, the normal force and shear force of each module are tested respectively. In order to realize 3D attitude-control and operation for AR application, a strategy combined the component vectors is proposed. According to the attitude in 3D space, the normal forces and shear forces detected by 8 electrodes simulate the space vector (X, Y, Z and θ_X, θ_Y, θ_Z). Through the combination of these six parameters, the transformation of any attitude in 3D space can be realized. Table 2 shows the relationship between 8 electrodes output instructions and six-axis attitude-control. In order to achieve accurate attitude operation, a threshold is set for the voltage output under conventional force operation. The voltage greater than the threshold is set to be "1". When (E1, E4) and (E1′, E4′) increase to the larger value than threshold because the contacting areas of two spheres are all on E1, E4 and E1′, E4′ respectively, it indicates the direction of X+. And there is no signal output at the other electrodes. Similarly, the larger values of (E2, E3) and (E2′, E3′) indicates direction X-. The representation of the Z direction is the same as X direction. The larger values of (E3, E4) and (E3′, E4′) indicates direction Z+. The larger values of (E1, E2) and (E1′, E2′) indicates direction Z-. The representation of the Y direction is different from X direction. The two symmetric modules determine the Y+ and Y- directions, separately. When the 4 electrodes (E1, E2, E3, E4) have the same value at the same time and the 4 electrodes (E1′, E2′, E3′, E4′) have no signals, it means the direction of Y-. Oppositely, when the 4 electrodes (E1′, E2′, E3′, E4′) have the same value at the same time, it means the direction of Y+. The larger values of (E1, E2) and (E3′, E4′) indicates the counter clockwise rotation attitude θ_X, and there is no signal output at the other electrodes. The largest values of (E3, E4) and (E1′, E2′) indicates the clockwise rotation direction θ_X-. The representation of the θ_Z direction is the same as θ_X direction. To indicate the θ_Y, the two fingers pinch the balls at the same time, then spin clockwise (or counter clockwise) around the Y axis. In Table 2, (E4, E3, E2, E1) and (E4′, E3′, E2′, E1′) have a time delay in turn using the arrow to show. This delay shows the motion is a counter clockwise rotation θ_Y+. On the contrary, it means θ_Y-.

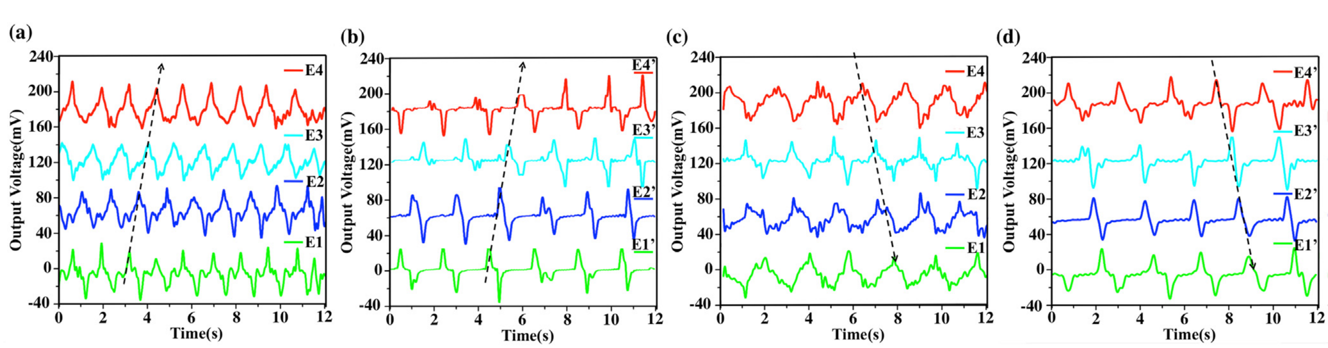

Fig. 7. Voltage waveforms of the rotation motions of each module. (a) The motion of a clockwise rotation of M-A at a high frequency. (b) The motion of a clockwise rotation of M-B at a low frequency. (c) The motion of a counter-clockwise rotation of M-A. (d) The motion of a counter-clockwise rotation of M-B.

Table 2
Output of the electrodes corresponding to the different operation instructions.

Direction and attitude	E1	E2	E3	E4	E’1	E’2	E’3	E’4
X	1			1	1			1
X-		1	1			1	1	
Y					1	1	1	1
Y-	1	1	1	1				
Z			1	1			1	1
Z-	1	1			1	1		
θ_X	1	1					1	1
θ_X-			1	1	1	1		
θ_Y	1	←		1	1	←		1
θ_Y-	1	→		1	1	→		1
θ_Z	1			1		1	1	
θ_Z-		1	1		1			1

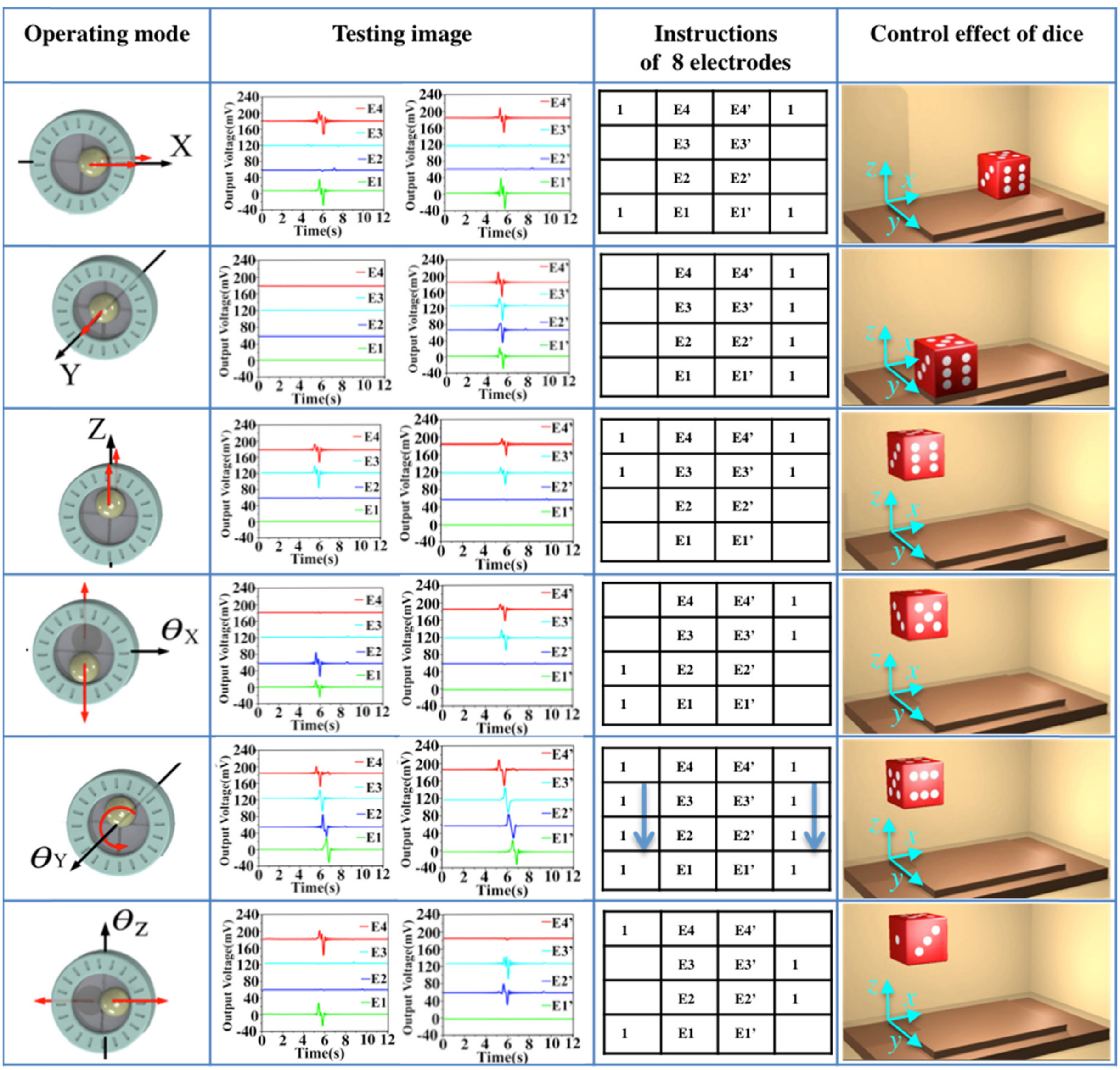

Fig. 8. The relationship between the six-axis operation strategy and the curve of voltages to control a dice for AR interface.

3.4. Demonstration of VR-3D-CS for VR control

To demonstrate the practical applicability of the VR-3D-CS, it is directly connected with A/D converter to control the virtual dice in virtual space as shown in Fig. 8. The sampling frequency of the A/D converter is 10 kHz and the precision of acquisition voltage is up to 0.01 mV. It can collect 8 channels at the same time. The converter is connected to the USB port of computer. In order to avoid the crosstalk between the 8 signals, it is mainly solved through two ways. Firstly, the A/D circuit in the convertor card uses differential input to suppress common mode interference. Then, in the experiment, a relatively high threshold trigger of the sensor in the software is set to distinguish the instructions and interference. The dice in virtual space is controlled by the corresponding output signals. The first column of Fig. 8 shows the operating modes of the sensor for X, Y, Z directions and revolving around the X, Y, Z axes, respectively. The second column shows the readout values of 8 channel voltages. The third column shows the instructions of 8 electrodes to control the dice. The fourth column shows the controlling effect of the dice in virtual space. The update rate of the protocol data used in this demonstration is less than 10 Hz, thus the response time is more than 0.1 s. In the software, the communication interval is set as 0.3 s for this demonstrate. (See Supporting Information Movie 2)

Supplementary material related to this article can be found online at http://dx.doi.org/10.1016/j.nanoen.2018.06.022.

From Table 2, it can be seen that the eight electrodes do not appear to be “1” at the same time. In order to improve the interactive effect of controlling object in AR interface, this function is fully used to realize the picking and releasing movements of the virtual object. When two fingers press two spheres into the middle at the same time, eight electrodes are “1” at the same time. This process is defined as single click, which means the picking movement of the virtual object. And the action of double clicks is set as the releasing movements as shown in Fig. 9(a)–(d).

In the above demonstration, the VR-3D-CS realizes the attitude control of a single object in virtual space. Among them, the VR is realized through the “Unity3D” development engine developed by Unity Technologies, combined with the C++ programming language. The program of Unity3D can run in the Windows environment. And it can also be exported to different display platforms and combined with VR devices such as VR glass, in which the virtual 3D effect can be achieved. The main components of the VR system are shown in Fig. S4 (Supporting information). Currently, Unity3D is the mainstream program to realize VR and AR [68,69]. In this paper, to highlight the control characteristics of the sensor and facilitate demonstration, the Windows environment in computer terminal is used to demonstrate the VR effect. To highlight the ability of the VR-3D-CS and expand its applications, the virtual assemble for AR interface is shown in Fig. 9(e)–(h). There are three parts to be assembled. The assembly process is divided into the following three steps. First step is that the part “A” is placed on the assembly platform. Then, part “B” is packed into the assemble hole of part “A”. At last , part “C” and part “B” are assembled according to the requirements. In the process of operation, the control instructions of parts correspond to the unit distance and unit angle on the six axes. With the pick and release instructions, three parts are operated in sequence, and the whole assembly process is completed (See Supporting information Movie 3). Experiments show that the VR-3D-CS can not only realize the attitude-control of a single object, but also realize the assembly of a number of objects. For the future application, the device can be improved in power and portability, and by optimizing structure, enabling the controlling with higher resolution.

Supplementary material related to this article can be found online at http://dx.doi.org/10.1016/j.nanoen.2018.06.022.

4. Conclusion

In summary, a VR-3D-CS is proposed and investigated with complete theoretical model and experimental characterization. The sensor can detect both the normal force and shear force, which can be used as AR interactive interface to realize 3D attitude-control operation of the objects. For detecting the normal force, it shows a linear range from 0 to 18 N. The open circuit voltage, output charge and short circuit current sensitivity are 3.6 V N^{-1}, 1.1 nC N^{-1} and 11.1 nA N^{-1}, respectively. In the aspect of shear force detection, it can resolve the shear force direction with step of at least 15°. The symmetric sensor modules are designed with 2 touch points and 8 sensing electrodes. The capability of detecting the normal force and the shear force is calibrated by judging voltage values of 8 electrodes. The combination of the 8 components simulates the space vector (X, Y, Z and θ_X, θ_Y, θ_Z). Thus, the sensor realized the 3D attitude-control operation of object in virtual space. Finally, demonstration of VR-3D-CS as interactive tool is successfully realized in the virtual assembly for AR application. Considering the advantages of self-powered mechanism, cost effectiveness, and easy implementation, the VR-3D-CS shows great potential for batteryless AR interface, robotics, and energy saving applications.

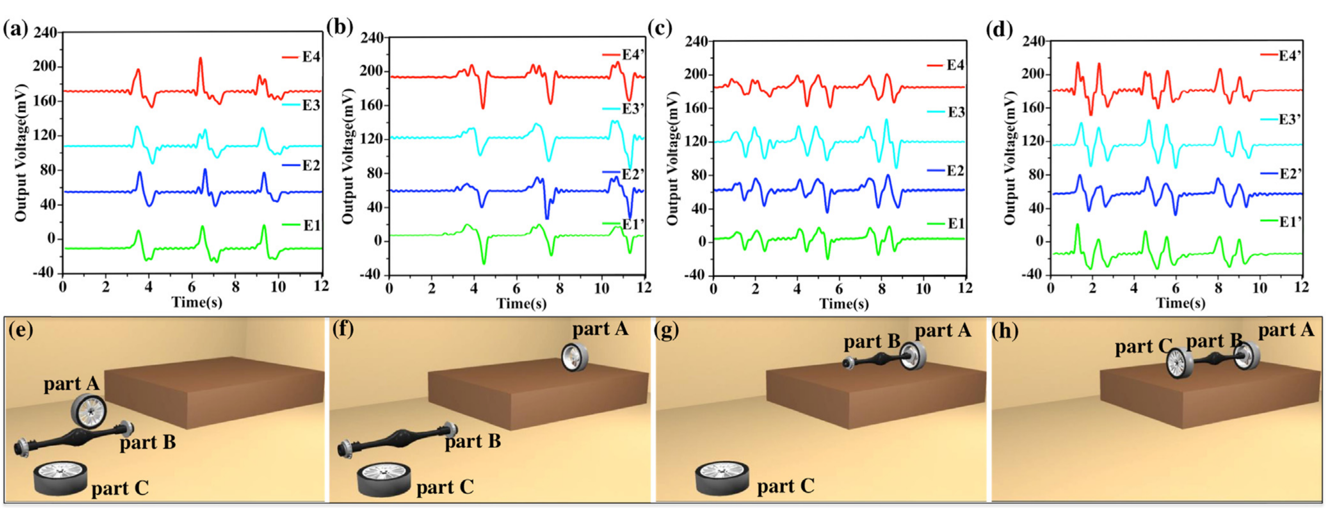

Fig. 9. The voltage curves of (a) M-A and (b) M-B with single click. The voltage curves of (c) M-A and (d) M-B with double clicks. Using the 3D self-powered sensor to realize the virtual assemble for AR interface. (e) The initial state. (f) The part A is put on the platform. (g) The virtual assemble of part B. (h) The virtual assemble of part C.

Acknowledgement

The authors acknowledge the financial support from the following research grants: National Natural Science Foundation of China Grant nos. 61673287 and 61433010; Ministry of Education (MOE) Faculty Research Committee (FRC) Grant (R-263-000-B56-112) "Thermoelectric Power Generator (TEG) Based Self-Powered ECG Plaster – System Integration (Part 3)" at the National University of Singapore; NRF-CRP8-2011-01 Grant (R-263-000-A27-281) "Self-Powered Body Sensor Network for Disease Management and Prevention Oriented Healthcare" by the National Research Foundation (NRF), Singapore; HIFES Seed Funding-2017-01 Grant (R-263-501-012-133) "Hybrid Integration of Flexible Power Source and Pressure Sensors".

Appendix A. Supporting information

Supplementary data associated with this article can be found in the online version at http://dx.doi.org/10.1016/j.nanoen.2018.06.022.

References

[1] K. Lee, Insight A J. Sch. Teach. 7 (2017) 31–42.
[2] T. Guan, L. Duan, Y. Chen, J. Yu, Sensors 10 (2010) 6017–6043.
[3] L. Yu, S.K. Ong, A.Y.C. Nee, Multimed. Tools Appl. 75 (2016) 1–22.
[4] W. Fang, L. Zheng, H. Deng, H. Zhang, Sensors 17 (2017) 1–22.
[5] W. Fang, L. Zheng, X. Wu, Comput. Ind. (2017) 91–103.
[6] D.P. Kaur, A. Mantri, IEEE Intern. Conference on Moocs, 2016, pp. 176–181.
[7] P. Fuchs, G. Moreau, P. Guitton, CRC Press, 2011.
[8] X.Y. Dong, Adv. Mater. Res. 791–793 (2013) 1208–1213.
[9] S. Yoshida, T. Mizota, H. Noma, IEEE Virtual Conference, 2007, pp. 281–282.
[10] H.J. Kwon, J.H. Kim, W.C. Choi, Microsyst. Technol. 17 (2011) 1721–1726.
[11] H. Chen, L. Miao, Z. Su, Y. Song, M. Han, X. Chen, X. Cheng, D. Chen, H.X. Zhang, Nano Energy 40 (2017) 65–72.
[12] X. Chen, Y. Song, H. Chen, J. Zhang, H.X. Zhang, J. Mater. Chem. A 5 (2017) 12361–12368.
[13] J. Zou, M. Zhang, J. Huang, J. Bian, Y. Jie, M. Willander, X. Cao, N. Wang, Z.L. Wang, Adv. Energy Mater. (2018).
[14] Y. Huang, H. Yuan, W.Q. Kan, X.H. Guo, C.X. Liu, P. Liu, Microsyst. Technol. 23 (2017) 1847–1852.
[15] F.R. Fan, Z.Q. Tian, Z.L. Wang, Nano Energy 1 (2012) 328–334.
[16] Z. Su, M. Han, X. Cheng, H. Chen, X. Chen, H.X. Zhang, Adv. Funct. Mater. 26 (2016) 5524–5533.
[17] Y. Ma, Q. Zhang, Y. Liu, B. Shi, X. Xue, W. Ji, Z. Liu, Y. Jin, Y. Zou, Z. An, W. Zhang, X. Wang, W. Jiang, Z. Xu, Z.L. Wang, H. Zhang, Nano Lett. 16 (2016) 6042–6051.
[18] G. Gu, C. Han, J. Tian, C. Lu, C. He, T. Jiang, Z. Li, Z.L. Wang, ACS Appl. Mater. Interfaces 9 (2017) 11882–11888.
[19] X. Liu, K. Zhao, Z.L. Wang, Y. Yang, Adv. Energy Mater. 7 (2017) 1701629.
[20] X. Pu, H. Guo, J. Chen, X. Wang, Y. Xi, C. Hu, Z.L. Wang, Sci. Adv. 3 (2017) e1700694.
[21] G. Liu, J. Chen, Q. Tang, L. Feng, H. Yang, J. Li, Y. Xi, X. Wang, C. Hu, Adv. Energy Mater. (2018) 1703086.
[22] J. Chen, X.J. Pu, H.Y. Guo, Q. Tang, L. Feng, X. Wang, C.G. Hu, Nano Energy 43 (2018) 253–258.
[23] L.B. Schein, Science 316 (2006) 1572–1573.
[24] T.A.L. Burgo, T.R.D. Ducati, K.R. Francisco, K.J. Clinckspoor, F. Galembeck, S.E. Galembeck, Langmuir 28 (2012) 7407–7416.
[25] Q. Zheng, H. Zhang, B. Shi, X. Xue, Z. Liu, Y. Jin, Y. Ma, Y. Zou, X. Wang, Z. An, W. Tang, W. Zhang, F. Yang, Y. Liu, X. Lang, Z. Xu, Z. Li, Z.L. Wang, ACS Nano 10 (2016) 6510–6518.
[26] T. Li, H. Luo, L. Qin, X. Wang, Z. Xiong, H. Ding, Y. Gu, Z. Liu, T. Zhang, Small 12 (2016) 5042–5048.
[27] H. Guo, T. Li, X. Cao, J. Xiong, Y. Jie, M. Willander, X. Cao, N. Wang, Z.L. Wang, ACS Nano 11 (2017) 856–864.
[28] S. Qi, H. Guo, J. Chen, J. Fu, C.G. Hu, M. Yu, Z.L. Wang, Nanoscale 10 (2018) 4745–4752.
[29] N. Zhang, C. Tao, X. Fan, J. Chen, J. Mater. Res. 32 (2017) 1628.
[30] R.K. Gupta, Q. Shi, L. Dhakar, T. Wang, C.H. Heng, C. Lee, Sci. Rep. 7 (2017) 41396.
[31] L. Dhakar, S. Gudla, X. Shan, Z. Wang, F.E.H. Tay, C.H. Heng, C. Lee, Sci. Rep. 6 (2016) 22253.
[32] H. Li, L. Su, S. Kuang, Y. Fan, Y. Wu, Z.L. Wang, G. Zhu, Nano Res. 10 (2017) 785–793.
[33] T. Li, J. Zou, F. Xing, M. Zhang, X. Cao, N. Wang, Z.L. Wang, ACS Nano 11 (2017) 3950–3956.
[34] Z.L. Wang, J. Chen, L. Lin, Energy Environ. Sci. 8 (2015) 2250.
[35] S. Cheon, H. Kang, H. Kim, Y. Son, J.Y. Lee, H.J. Shin, S.W. Kim, J.H. Cho, Adv. Funct. Mater. 28 (2017) 1703778.
[36] H.J. Choi, J.H. Lee, J. Jun, T.Y. Kim, S.W. Kim, H. Lee, Nano Energy 27 (2016) 595–601.
[37] R. Hinchet, A. Ghaffarinejad, Y. Lu, J.Y. Hasani, S.W. Kim, P. Basset, Nano Energy 47 (2018) 401–409.
[38] H. Wang, H. Wu, D. Hasan, T. He, Q. Shi, C. Lee, Acs Nano 11 (2017) 10337–10346.
[39] Q. Shi, H. Wu, H. Wang, H. Wu, C. Lee, Adv. Energy Mater. 7 (2017) 1701300.
[40] T. Chen, Y. Xia, W. Liu, H. Liu, L. Sun, C. Lee, J. MEMS 12 (2016) 845–847.
[41] H. Liu, T. Chen, L. Sun, C. Lee, Micromachines 6 (2015) 984–992.
[42] F. Wang, Z. Liu, P. Zhang, H. Li, W. Sheng, T. Zhang, R. Jordan, Y. Wu, X. Zhang, X. Feng, Small 13 (2017) 1702449.
[43] J.W. Zhong, Q. Zhang, F.R. Fan, Y. Zhang, S.H. Wang, B. Hu, Z.L. Wang, J. Zhou, Nano Energy 2 (2012) 491–497.
[44] Y. Yang, H. Zhang, X. Zhong, F. Yi, R. Yu, Y. Zhang, Z.L. Wang, ACS Appl. Mater. Interfaces 6 (2014) 3680–3688.
[45] U. Khan, T.H. Kim, H. Ryu, W. Seung, S.W. Kim, Adv. Mater. 29 (2017) 1603544.
[46] Q. Jing, G. Zhu, W. Wu, P. Bai, Y. Xie, R.P. Han, Z.L. Wang, Nano Energy 10 (2014) 305.
[47] Y. Yang, H. Zhang, Z.H. Lin, Y.S. Zhou, Q. Jing, Y. Su, J. Yang, J. Chen, C. Hu, Z.L. Wang, ACS Nano 7 (2013) 9213–9222.
[48] G.H. Lim, S.S. Kwak, N. Kwon, T. Kim, H. Kim, S.M. Kim, S.W. Kim, B. Lim, Nano Energy 42 (2017) 300–306.
[49] Y. Cao, T. Li, Y. Gu, H. Luo, S. Wang, T. Zhang, Small (2018).
[50] L. Su, H.Y. Li, Y. Wang, S. Kuang, Z.L. Wang, G. Zhu, Nano Energy 31 (2017) 264–269.
[51] Y. Yang, Y.S. Zhou, H. Zhang, Y. Liu, S. Lee, Z.L. Wang, Adv. Mater. 25 (2013) 6594.
[52] G. Zhu, W.Q. Yang, T. Zhang, Q. Jing, J. Chen, Y.S. Zhou, P. Bai, Z.L. Wang, Nano Lett. 14 (2014) 3208.
[53] F. Yi, L. Lin, S. Niu, J. Yang, W. Wu, S. Wang, Q. Liao, Y. Zhang, Z.L. Wang, Adv. Funct. Mater. 24 (2014) 7488.
[54] Q. Shi, H. Wang, T. Wang, C. Lee, Nano Energy 30 (2016) 450.
[55] B. Meng, W. Tang, Z.-H. Too, X. Zhang, M. Han, W. Liu, H. Zhang, Energy Environ. Sci. 6 (2013) 3235.
[56] X. He, Y. Zi, H. Yu, S.L. Zhang, J. Wang, W. Ding, H. Zou, W. Zhang, C. Lu, Z.L. Wang, Nano Energy 39 (2017) 328.
[57] Z. Wang, R. Jiang, G. Li, Y. Chen, Z. Tang, Y. Wang, Z. Liu, H. Jiang, C. Zhi, ACS Appl. Mater. Interfaces 9 (2017) 22685.
[58] X. Zhang, Y. Zheng, D. Wang, F. Zhou, Nano Energy 40 (2017) 95.
[59] Z.L. Wang, Faraday Discuss. 176 (2014) 447.
[60] D. Davies, J. Phys. D: Appl. Phys. 2 (1969) 1533.
[61] A. Wåhlin, G. Bäckström, J. Appl. Phys. 45 (1974) 2058.
[62] D. Armani, C. Liu, N. Aluru, Twelfth IEEE International Conference on presented at Micro Electro Mechanical Systems, MEMS'99, 1999.
[63] P. Rae, E. Brown, Polymer 46 (2005) 8128.
[64] W.M. Haynes, CRC Handbook of Chemistry and Physics, CRC Press, Boca Raton, FL, USA, 2014.
[65] S. Trigwell, J. Captain, J. Captain, E. Arens, J. Quinn, C. Calle, Trigwell Steve (2006).
[66] J.G. Speight, Lange's Handbook of Chemistry, McGraw-Hill, New York, 2005.
[67] P.A. Tipler, R. Llewellyn, Modern Physics, Macmillan, New York, USA, 2003.
[68] S. Wang, D.B. Lian, Y. Chen, Comput. Syst. Appl. 25 (2016) 72–76.
[69] K. Jiang, F.Y. Zheng, H.K. Tang, Appl. Mech. Mater. 602 605 (2014) 1838–1841.

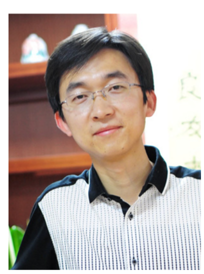

Tao Chen received the B.Sc. degree in Mechanical Design, Manufacturing and Automation, M.Sc. degree in Mechatronic Engineering, and Ph.D. degree in Mechatronic Engineering from Harbin Institute of Technology, Harbin, China, in 2004, 2006, and 2010, respectively. He is a visiting scholar in National University of Singapore in 2018. He is currently an associate professor at Soochow University, Suzhou, China. His main research interests include MEMS, sensors, and actuators.

Mingyue Zhao received her B.Eng. degree in School of Information and Electronics from Beijing Institute of Technology (BIT) in 2017 and M.Sc degree in Department of Electrical and Computer Engineering (ECE), National University of Singapore (NUS) in 2018. Her research interests are focused on virtual reality and augmented reality.

Qiongfeng Shi received his B.Eng. degree from Department of Electronic Engineering and Information Science at University of Science and Technology of China (USTC) in 2012. He is currently pursuing his Ph.D. degree in the Department of Electrical and Computer Engineering, National University of Singapore (NUS) under the NUS research scholarship. His research interests are focused on energy harvesters and self-powered sensors.

Zhan Yang received B.S.in department of automation in Harbin University of Science and Technology, M.S. and Dr. Eng. in department of micronano system of Nagoya University in 2010 and 2013. He is Associate Professor in Robotics and Microsystem Center, Soochow University, Suzhou, China and Collaborative Innovation Center of Suzhou Nano Science and Technology, Soochow University. He is Secretary-General of China Society of Micro-Nano Robotics. His research interest in nano manipulation, nano sensor and nano robotics. He has published more than 30 papers on micronano manipulation and their applications.

Huicong Liu received her Ph.D. degree from the Department of Mechanical Engineering, National University of Singapore (NUS) in 2013. She has been a Research Fellow in Department of Electrical and Computer Engineering, NUS from Aug. 2012 to Aug. 2013. Currently she is an Associate Professor in Robotics and Microsystems Center, School of Mechanical & Electric Engineering, Soochow University, China. Her research interests are vibration-based MEMS/NEMS energy harvesters, self-powered MEMS/NEMS system for IoTs and flexible functional devices for robotic and medical applications.

Lining Sun is currently a director of Robotics and Microsystems Center in Soochow University, and a President of College of Mechatronic Engineering in Soochow University. He gained China National Funds for Distinguished Young Scientists. His current research interests include micro-nano operational robot and equipment, advanced robot and control, and electromechanical integration equipment. He gained two National Science and Technology Award Grade II and three Provincial Science and Technology Prize Grade I. He has more than 300 academic papers being published and has more than 20 patents of invention being authorized.

Jianyong Ouyang received his Ph.D., master and bachelor degrees from the Institute for Molecular Science in Japan, the Institute of Chemistry of the Chinese Academy of Science, and the Tsinghua university in Beijing, respectively. He worked as an assistant professor at the Japanese Advanced Institute of Science and Technology and a postdoctoral researcher at the University of California, Los Angeles (UCLA) before joining the National University of Singapore as an assistant professor in 2006. He was promoted to associate professor in 2012. His research interests include flexible electronics and energy materials and devices.

Chengkuo Lee received his Ph.D. degree in Precision engineering from The University of Tokyo in 1996. Currently, he is the director of Center for Intelligent Sensors and MEMS, and an Associate Professor in the Department of Electrical and Computer Engineering, National University of Singapore, Singapore. In 2001, he cofounded Asia Pacific Microsystems, Inc., where he was the Vice President. From 2006 to 2009, he was a Senior Member of the Technical Staff at the Institute of Microelectronics, A-STAR, Singapore. He has contributed to more than 250 peer-reviewed international journal articles, and 300 international conference papers and extended abstracts.